RESEARCH

Targeting tumor–stromal interactions in triple-negative breast cancer using a human vascularized micro-tumor model

Stephanie J. Hachey[1*†], Christopher J. Hatch[2†], Daniela Gaebler[1], Aneela Mocherla[1], Kevin Nee[3], Kai Kessenbrock[3] and Christopher C. W. Hughes[1,2]

Abstract

Triple-negative breast cancer (TNBC) is highly aggressive with limited available treatments. Stromal cells in the tumor microenvironment (TME) are crucial in TNBC progression; however, understanding the molecular basis of stromal cell activation and tumor–stromal crosstalk in TNBC is limited. To investigate therapeutic targets in the TNBC stromal niche, we used an advanced human in vitro microphysiological system called the vascularized micro-tumor (VMT). Using single-cell RNA sequencing, we revealed that normal breast tissue stromal cells activate neoplastic signaling pathways in the TNBC TME. By comparing interactions in VMTs with clinical data, we identified therapeutic targets at the tumor–stromal interface with potential clinical significance. Combining treatments targeting Tie2 signaling with paclitaxel resulted in vessel normalization and increased efficacy of paclitaxel in the TNBC VMT. Dual inhibition of HER3 and Akt also showed efficacy against TNBC. These data demonstrate the potential of inducing a favorable TME as a targeted therapeutic approach in TNBC.

Keywords Triple-negative breast cancer, Tumor microenvironment, Microphysiologic system

Introduction

Triple-negative breast cancer (TNBC), representing approximately 15% of all breast carcinomas, is an aggressive disease with limited treatment options [1]. Consequently, TNBC disproportionally accounts for 30% of all breast cancer-related mortality, with approximately 150,000 deaths estimated in 2023 [2]. Since TNBC, by definition, lacks expression of the estrogen receptor

(ER), progesterone receptor (PR), and human epidermal growth factor receptor 2 (HER2), chemotherapy remains standard for systemic treatment, as endocrine therapy and HER2-directed therapies are ineffective [3]. Compared with hormone receptor (HR)-positive breast cancer, TNBC is more commonly diagnosed in women younger than 40 years and has a worse 5-year survival rate [3]. A study evaluating 15,204 women who presented with stage I–III breast cancer at National Comprehensive Cancer Network Centers found that women with TNBC experienced worse breast cancer-specific and overall survival (OS) in multivariate analyses (OS: adjusted hazard ratio, 2.72; 95% confidence interval 2.39–3.10; $p < 0.0001$) compared to women with HR-positive/HER2-negative breast cancer [4]. Additionally, TNBC tumors have been found to be associated with unique risk factors and poor prognosis, including an increased risk of death within 2 years of diagnosis [4], highlighting the

†Stephanie J. Hachey and Christopher J. Hatch contributed equally to this work.

*Correspondence:
Stephanie J. Hachey
shachey@uci.edu
[1] Molecular Biology and Biochemistry, University of California, Irvine, Irvine, CA, USA
[2] Biomedical Engineering, University of California, Irvine, Irvine, CA, USA
[3] Biological Chemistry, University of California, Irvine, Irvine, CA, USA

Hachey *et al. Breast Cancer Research*   (2024) 26:5

Page 2 of 20

need to develop more effective treatments for this deadly malignancy.

Current first-line therapy for patients with TNBC includes neo/adjuvant anthracycline-, alkylator-, and taxane-based chemotherapy regimens, for example doxorubicin and cyclophosphamide followed by paclitaxel [5]. However, chemotherapy achieves a complete response in only about 30% of TNBC patients, and more than 50% of patients experience relapse within the first 3–5 years due to the development of therapy resistance. Additionally, patients with stage IV TNBC treated with standard-of-care chemotherapy have a median overall survival of just 10.2 months [5]. There is growing evidence that stromal cells in the tumor microenvironment (TME) play an important role in cancer progression and treatment resistance in TNBC [5–9] and are therefore considered a potential therapeutic target. The TME, a major determinant of cancer phenotype, is a complex and heterogeneous ecosystem co-opted by neoplastic cells, consisting of both cancerous and nonmalignant cell populations embedded in a glycoprotein-rich extracellular matrix (ECM). Cancer-associated fibroblasts (CAFs) are a prominent component of the tumor stroma from which gene expression signatures have been found to strongly predict TNBC prognosis. Upregulated pathways include those associated with ECM remodeling and chemokine signaling, which contribute to tumor cell growth and invasion as well as vascular destabilization [10–12]. However, the underlying molecular mechanisms driving stromal cell activation and the reciprocal communication between tumor cells and stromal cells in TNBC remain poorly understood, impeding the development of targeted therapies focused on the stromal component.

In this study, our aim was to uncover mechanisms by which the microenvironment of TNBC triggers the reprogramming of stromal cells into an activated state, ultimately influencing both tumor growth and response to therapy. Additionally, we aimed to identify and evaluate potential therapeutic targets for TNBC. Herein we establish human vascularized micro-tumor (VMT) models to recreate the TNBC TME in vitro, using primary stromal cells isolated freshly from healthy human breast tissue, endothelial cells (ECs) and two representative TNBC cell lines, HCC1599 and MDA-MB-231. The VMT is a microphysiologic in vitro cancer model that we have validated for disease modeling, drug screening and personalized medicine applications for solid tumors [13–17]. By co-culturing multiple cell types within a complex ECM under dynamic flow conditions, the stromal cells and endothelium spontaneously self-organize into a perfused vascular network that plays a vital role in supporting tumor growth and serves as a physiological conduit for the delivery of therapeutic agents to the tumor. Furthermore, the VMT accurately replicates key characteristics of an in vivo tumor, including the presence of irregular and poorly perfused tumor-associated vasculature, which can hinder the effective delivery of therapeutics to the tumor and contribute to treatment resistance [16].

By leveraging single-cell RNA sequencing (scRNA-seq), we investigated gene expression patterns, cellular heterogeneity, and intercellular communication within TNBCs. Vascularized micro-organs (VMOs), healthy tissue constructs containing endothelial cells and stroma without tumor, were established as controls. Our analysis revealed that histopathologically normal human breast tissue-derived stromal cells activate neoplastic signaling pathways when exposed to the TNBC TME. Through a comparison of these interactions in VMTs with scRNA-seq data obtained from clinical specimens, we successfully identified therapeutic targets situated at the tumor–stromal interface that hold potential clinical significance.

Results

Healthy breast tissue-derived stromal cells support microvascular network formation in VMO and VMT models

For physiologic modeling of TNBC, primary-derived stromal cells were freshly isolated from histopathologically normal (healthy, noncancerous) breast tissue under an IRB-approved protocol and tested for vascular network formation in VMO/VMTs (Fig. 1). VMOs and VMTs are established within a microfluidic device (Fig. 1A) via co-culture of multiple cell types within an extracellular matrix. Cells are introduced into the tissue chamber of each unit through the loading port (L1 or L2) and experience dynamic flow via a hydrostatic pressure gradient through the microfluidic channels from the media reservoirs (M1–M2 and M3–M4). In response to flow across the tissue chamber, ECs and stromal cells self-assemble into a microvascular network by day 5 of culture to allow in vivo-like delivery of nutrients and drugs to the tissue.

As shown in Fig. 1B, healthy breast tissue-specific primary stromal cells (shown in blue) support the development of microvessels (red) that are fully perfused by 70 kDa fluorescent dextran (cyan). Matched VMOs and VMTs containing TNBC cell lines MDA-MB-231 and HCC1599 (shown in green) were established (Fig. 1C). MDA-MB-231 grows rapidly with stellate morphology and manifests invasive spread within the VMT, gradually disrupting the surrounding vasculature over time. In contrast, HCC1599 exhibits slow proliferation as 3D clusters and has been demonstrated to closely resemble clinical TNBC samples in terms of various molecular
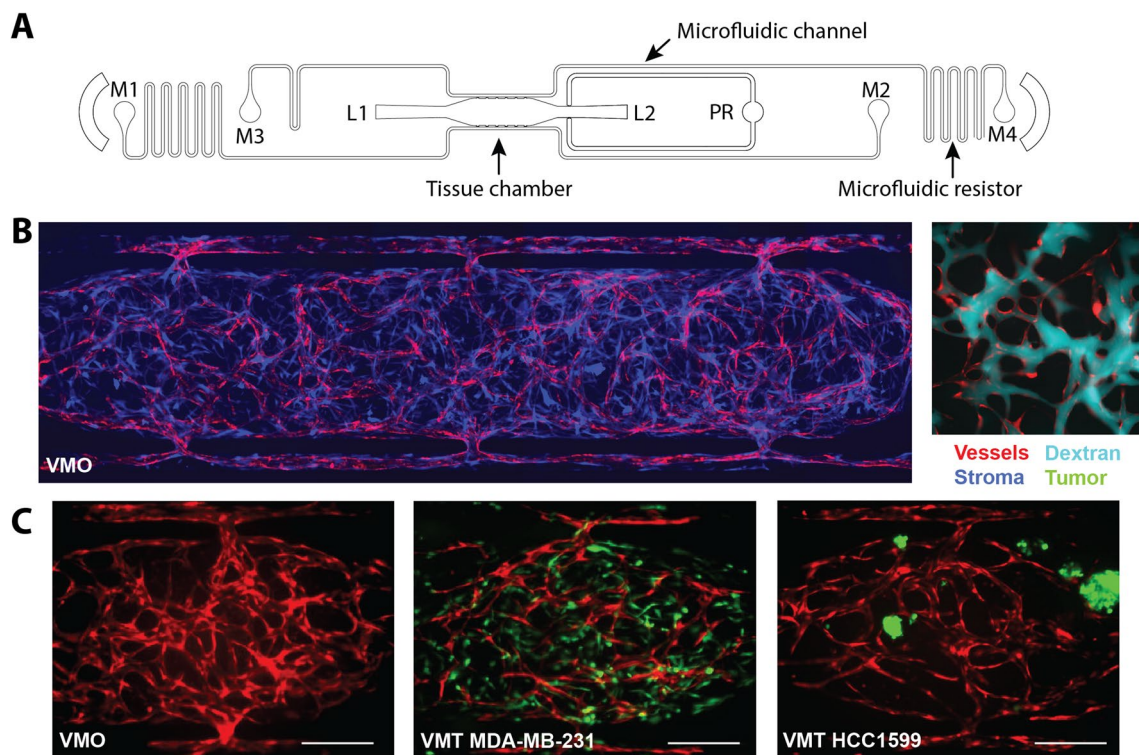
Fig. 1 Stromal cells freshly isolated from healthy breast tissue support microvascular network formation in VMO and VMT models. **A** Schematic of a single device unit with a single tissue chamber fed through microfluidic channels, 2 loading ports (L1–2), and uncoupled medium inlet and outlets (M1–2 and M3–4). A pressure regulator (PR) serves as a burst valve to release excess pressure from the tissue chamber during loading. **B** Left: Fluorescent image of a VMO established with stromal cells isolated freshly from histopathologically normal breast tissue. Vessels are shown in red and primary fibroblasts in blue. Right: Zoom view of a vascular network (red) perfused with 70 kDa dextran (cyan). **C** Left panel: VMO established with patient-derived breast tissue stromal cells. Vasculature shown in red. Middle panel: VMT established with MDA-MB-231 TNBC cells and patient-derived stromal cells. Note invasiveness of the tumor cells. Vasculature is red, tumor is green, and stromal cells are unlabeled. Right panel: VMT established with HCC1599 TNBC cells and patient-derived stromal cells. Vasculature is red, tumor is green, and stromal cells are unlabeled. Scale bar = 200 μm

characteristics, such as gene expression signatures and copy number variations [18, 19].

Single-cell RNA sequencing reveals differential pathway activation in TNBC VMTs and VMOs

In order to gain deeper insights into the alterations of the vascular niche in TNBC tumors, we conducted scRNA-seq on cells isolated from TNBC VMTs (MDA-MB-231 and HCC1599) and their corresponding VMOs (vasculature and stroma in the absence of tumor cells; Fig. 2A). Using the SCTransform Seurat pipeline [20], we performed clustering analysis and confirmed distinct clusters corresponding to ECs, various stromal cells, and, in the case of TNBC VMTs, tumor cells for each dataset (Fig. 2B–I). The identification of cell types was determined based on top differentially expressed genes and the

(See figure on next page.)
Fig. 2 Single-cell RNA sequencing reveals transcriptomic shifts in triple-negative breast cancer VMTs and VMOs. **A** Schematic showing workflow of scRNA-seq. Matched VMO and VMT were established for TNBC cell lines MDA-MB-231 and HCC1599. Cells were isolated from each model and submitted for scRNA-seq. **B** UMAP of VMO matched to MDA-MB-231 VMT shows endothelial cells (ECs), fibroblasts, cycling cells and stromal cells are present as **C** shown with the expression of key marker genes. **D** UMAP of MDA-MB-231 VMT shows ECs, fibroblasts, stromal cells, cycling cells and tumors are present as **E** demonstrated with the expression of key marker genes. **F** UMAP of VMO matched to HCC1599 shows ECs, fibroblasts, and stromal cells are present as **G** demonstrated with the expression of key marker genes. **H** UMAP of HCC1599 VMT shows ECs, fibroblasts, stromal cells, and tumors are present as **I** shown with the expression of key marker genes. **J** Integrated dataset containing all cells from the VMO (MDA-MB-231), VMO (HCC1599), MDA-MB-231 VMT and HCC1599 VMT. **K** Proportions of different cell types from each dataset. **L** Heatmap showing top 5 DEGs from each cell type from each dataset in the integrated space
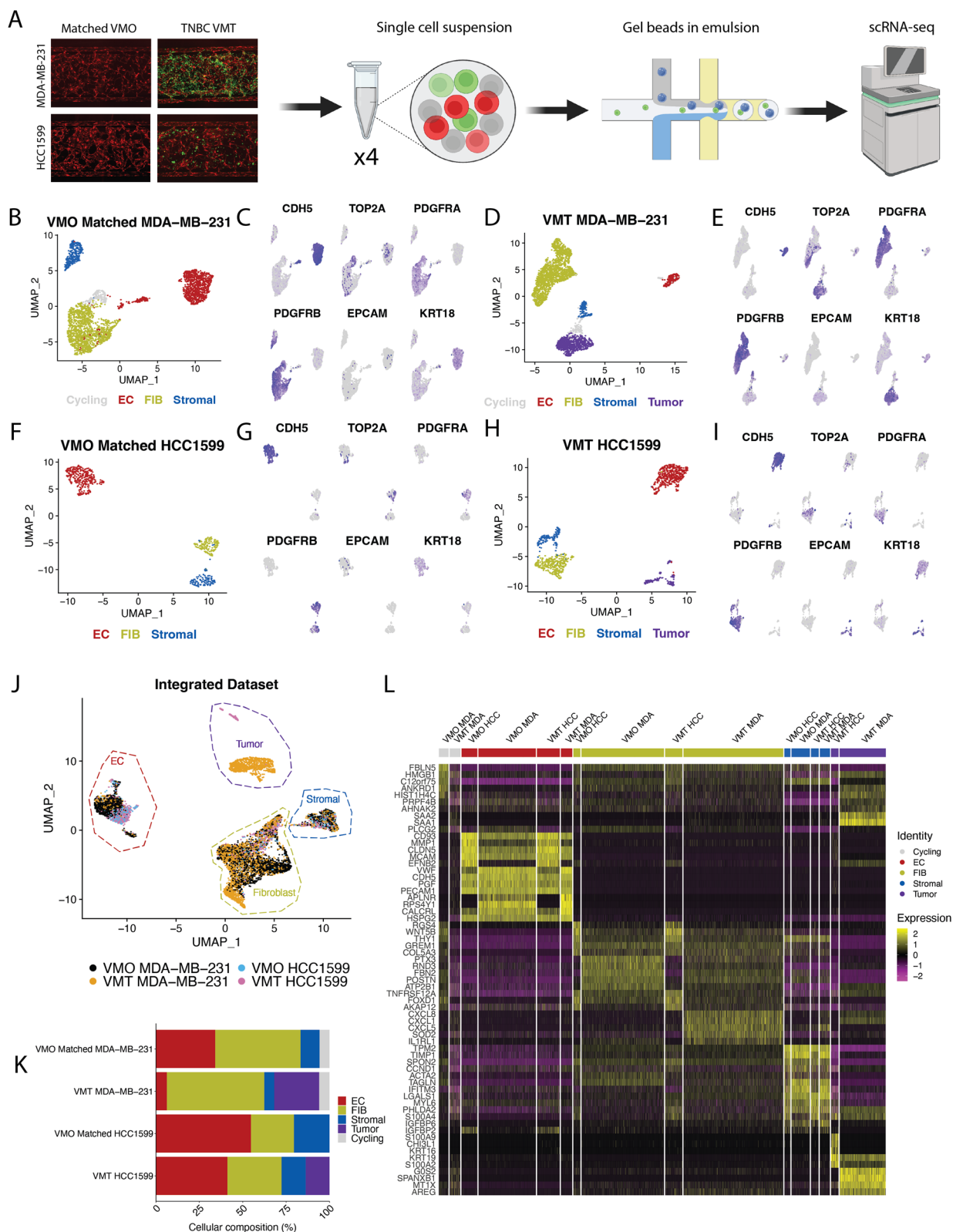
Hachey *et al. Breast Cancer Research*   (2024) 26:5

Page 4 of 20

Fig. 2 (See legend on previous page.)

Hachey *et al. Breast Cancer Research*   (2024) 26:5

Page 5 of 20

expression of known marker genes specific to each cell type. These included, but were not limited to: *PECAM1* and *CDH5* (EC markers), *PDGFRA* (fibroblast marker), *PDGFRB* (pericyte marker), and *EPCAM* and *KRT18* (cancer cell markers). Additionally, the matched MDA-MB-231 VMT and VMO datasets exhibited a population of cycling cells characterized by increased expression of *TOP2A* (Fig. 2B–E). Although there are slight differences in the UMAP and clustering results between the two VMOs (each VMO established at the same time as its matched VMT—MDA-MB-231 or HCC1599 VMTs), likely due to batch effects, integration of the datasets using scMC [21] reveals a seamless overlap between the cell populations (Additional file 1: Fig. A1A). Both VMOs show representation of ECs, fibroblasts, and stromal cells (Additional file 1: Fig. A1B), demonstrating that there were no significant differences between the VMOs.

Next, to examine the variations between datasets, all four datasets were integrated using scMC [21]. Unsupervised clustering of the integrated data revealed distinct clusters corresponding to the cell identities defined in the individual datasets, with clear separation of tumor cell lines (Fig. 2J). When analyzing the proportion of cell types contributed by each sample, we observed an increase in the percentage of fibroblasts and cancer cells in MDA-MB-231 VMTs compared to HCC1599 VMTs, accompanied by a decrease in the number of ECs (Fig. 2K). Comparing VMTs with VMO controls, HCC1599 VMT exhibited a marginal decrease in the number of endothelial cells, while MDA-MB-231 VMT displayed a significant decrease. These findings support the phenotypic results, where we observed a significant disruption and pruning of tumor-associated vasculature in the presence of MDA-MB-231 TNBC. That said, a heatmap depicting the top five differentially expressed genes for each cell type across datasets did demonstrate consistent upregulation of *VWF* and *CLDN5* among ECs (Fig. 2L, Additional file 2: Table S1). On the other hand, in contrast to HCC1599 VMT and VMOs, fibroblasts from MDA-MB-231 VMTs exhibited heightened expression of pro-inflammatory markers, including *CXCL1*, *CXCL5*, *CXCL8*, and *IL1RL1*.

Differential gene expression analyses of individual datasets reveal distinct pathway activation dependent on cell type in both VMTs and VMOs

Both VMTs and their corresponding VMO controls demonstrate cell-type-specific gene expression and pathway activation with some distinctions (Additional file 1: Fig. A1C–F, Additional file 3: Table S2). Notably, MDA-MB-231 VMT ECs have increased cell and tissue migration and a marginal decrease of angiogenesis, most prominently noted by a lack of CXCR4, which is essential

for EC tube formation [22] (Additional file 1: Fig. A1G). Although both VMO and VMT fibroblasts regulate their surrounding ECM, one gene that is unique to the VMT population is MMP2, which has been shown to have increased expression in the presence of breast cancer [23] (Additional file 1: Fig. A1H). In addition, the VMT stromal cells express genes known to increase neutrophil activation, which may support the dual role of neutrophil activation in promoting and suppressing cancer in vivo [24] (Additional file 1: Fig. A1I). Lastly, in the MDA-MB-231 VMT, the cycling cluster is enriched for RNA splicing, for which pathway alterations have been implicated in many human cancers (Additional file 1: Fig. A1J).

In the HCC1599 VMT, the ECs exhibited a stronger influence on extracellular matrix organization, driven by increased expression of *MMP1/2* (Additional file 1: Fig. A1). The HCC1599 VMT fibroblasts demonstrated deficiencies in regulating angiogenesis, as evidenced by the lack of expression of SPHK1, which has been shown to be necessary for supporting endothelial tube cell formation [25] (Additional file 1: Fig. A1). Additionally, the HCC1599 VMT fibroblasts exhibited increased expression of Inhibin Beta-A (INHBA), which has been implicated in epithelial–mesenchymal transition (EMT) and correlated with decreased breast cancer survival [26]. In contrast, stromal cells in the VMO control for the HCC1599 VMT exhibited better regulation of the ECM, with increased expression of *COL1A1* and *TGFBI*, both crucial for supporting lumen formation [27].

Tumor-specific analysis highlights differences in TNBC cell populations within the VMT

To focus on TNBC cell populations within the VMT, we integrated the MDA-MB-231 VMT and HCC1599 VMT datasets and subset the tumor cells from the EPCAM+ or KRT18+ clusters in the individual datasets for further investigation. Through unbiased clustering, we discovered heterogeneity within the tumor populations in both MDA-MB-231 and HCC1599, resulting in three distinct populations in MDA-MB-231 and two populations in HCC1599 (Additional file 1: Fig. A2A). Differential gene expression analysis revealed notable differences among the cellular populations within both MDA-MB-231 and HCC1599 VMT models (Additional file 1: Fig. A2B). Interestingly, in MDA-MB-231 TNBC, we observed a subset of cancer cells with a transcriptional profile resembling that of stromal cells. These cells exhibited increased expression of matrix-associated genes such as collagens (*COL1A1, COL1A2, COL3A1, COL6A1, COL6A2, COL6A3*) and fibronectin (*FN1*). Correspondingly, pathway analysis revealed an enrichment of processes related to extracellular matrix organization, collagen fibril

organization, and cell–substrate adhesion (Additional file 1: Fig. A2C).

The cycling population of MDA-MB-231 demonstrated elevated expression of *MKI67* and *TOP2A*, along with pathway enrichment associated with cell proliferation, including nuclear division and spindle organization (Additional file 1: Fig. A2D). The TNBC population of MDA-MB-231 exhibited upregulation of *AMIGO2*, which is implicated in cancer metastasis [28], and enhanced translational initiation (Additional file 1: Fig. A2E). Strikingly, and in contrast to published expression data from monolayer cultures [29, 30], MDA-MB-231 cells growing in the VMT lacked expression of the epithelial marker *EPCAM*, indicating transcriptional consistency with the invasive and migratory phenotype of MDA-MB-231 in the VMT. In contrast, HCC1599-1 displayed increased expression of basal epithelial markers (cytokeratins *KRT14*, *KRT15*, *KRT16*, *KRT17*) and *EPCAM*, accompanied by enrichment for keratinization processes (Additional file 1: Fig. A2F). HCC1599-2 exhibited pathway enrichment associated with positive regulation of vascular development and extracellular matrix organization (Additional file 1: Fig. A2G), aligning with the tumor growth and vascular morphology patterns observed in HCC1599 VMT.

A population of cells with a cancer-associated fibroblast (CAF) gene signature emerges from healthy breast tissue-derived stroma in MDA-MB-231 VMT

By subsetting fibroblasts from the integrated dataset, a distinct cellular population exhibiting a gene signature associated with cancer-associated fibroblasts (CAFs) emerges from the healthy breast tissue-derived stroma (Additional file 1: Fig. A3A) and demonstrates enrichment within the MDA-MB-231 VMT (Additional file 1: Fig. A3B). Notably, the MDA-MB-231 VMT displays an increased proportion of synthetic fibroblasts, while the HCC1599 VMT exhibits a significant enrichment of cycling fibroblasts (Additional file 1: Fig. A3B). Expression profiles of differentially expressed genes included: cycling cells (*TOP2A*, *MKI67*), fibroblasts (*GATA3*, *FLRT2*), synthetic fibroblasts (synthetic) (*COL1A1*, *PCOLCE*, *SPARC*, *IGFBP7*), and cancer associated fibroblasts (CAFs) (*CCL2*, *CXCL8*, *MMP2*) (Additional file 1: Fig. A3C, Additional file 4: Table S3). As shown in Additional file 1: Fig. A3D, additional CAF markers *AEBP1*, *COL11A1*, *COL12A1*, *CXCL1*, *EDNRA*, and *FAP* [12] are upregulated in the CAF population compared to the other fibroblast types. Differential gene expression analyses further revealed distinct patterns in gene transcription among different fibroblast subtypes (Additional file 1: Fig. A3E).

CAFs exhibited heightened expression of CAF-associated genes, such as *SERPINE2* and *MMP2*, which are involved in cell chemotaxis and extracellular matrix (ECM) remodeling (Additional file 1: Fig. A3F). Conversely, synthetic fibroblasts displayed elevated expression of genes related to ECM organization and collagen deposition, including *COL1A1/2*, *COL3A1*, *COL4A1*, and *COL5A1/3* (Additional file 1: Fig. A3G). Cycling fibroblasts exhibited increased expression of cell cycle genes and demonstrated enrichment in mitotic processes (Additional file 1: Fig. A3H). Moreover, fibroblasts exhibited upregulation of *FGF2* and biological pathways associated with responses to nutrients and external stimuli (Additional file 1: Fig. A3I).

Pseudotime analysis of the EC subset unveils a tumor-associated EC signature enrichment within the MDA-MB-231 VMT

A comparative analysis of ECs in the MDA-MB-231 VMT and corresponding VMO scRNA-seq datasets identified pathways that potentially contribute to the observed vascular disruption in the VMT (Additional file 1: Fig. A4). The ECs from both the VMO and VMT datasets were subset and integrated using scMC [21]. Through unsupervised clustering, three distinct clusters were identified (Additional file 1: Fig. A4A and B): one primarily composed of cells from VMO (EC_Normal), another predominantly composed of cells from VMT (EC_Tumor), and a third cluster consisting of cells from both datasets (EC_Cycling). Pathway analysis conducted on the EC_Normal group revealed an increased activity of receptor–ligand interactions and solute carrier family genes associated with the transport of substances across the plasma membrane (Additional file 1: Fig. A4C). Conversely, the EC_Tumor group exhibited elevated matrix metalloproteinase (MMP) activity, as well as cytokine and chemokine activity, suggesting that these ECs may disrupt the surrounding vascular niche (Additional file 1: Fig. A4D). Lastly, a shared group of cells appeared to be proliferating or cycling (Additional file 1: Fig. A4E).

ECs from MDA-MB-231 VMT and corresponding VMO were mapped onto a pseudotime using Monocle v2 (Additional file 1: Fig. A4F). The three EC clusters were further subdivided across five branch points (Additional file 1: Fig. A4F–G). Of particular interest was one branch in the pseudotime trajectory, primarily composed of cells from the tumor (Additional file 1: Fig. A4F, branch marked with asterisks). To gain deeper insights into the genes influencing this branch and causing its divergence, thereby driving the trajectory split, we performed branch expression analysis modeling (BEAM) using Monocle. For this analysis, branch point two was chosen as the reference for comparing gene expression. BEAM employs

two negative binomial general linear models to assess the likelihood of a gene being branch-specific [31]. This approach helps identify genes contributing to a specific branch. The genes associated with the EC tumor branch (see Additional file 1: Fig. A4H, right-hand side of heatmap) exhibited significant overlap with those identified during pathway analysis, including several MMPs and ADAMTS genes. This finding further highlights the disruption of the vascular niche due to interactions between ECs and MDA-MB-231 TNBC cells.

Tumor–stromal drug targets were identified by analyzing integrated datasets from VMO to VMT

To further elucidate the transcriptomic shifts between matched VMO and VMT datasets, each pair was integrated with scMC [21] (Additional file 1: Fig. A5). Integration of MDA-MB-231 VMT and its matched VMO datasets revealed five cell types: ECs, fibroblasts, pericytes, tumor, and cycling cells, as confirmed by the expression of known marker genes (Additional file 1: Fig. A5A and B). In order to identify dysregulated cell–cell communication that might be impacting the vascular niche, we employed LIANA [32] on the individual datasets. LIANA runs multiple cell–cell communication pipelines and compiles the results. The cell–cell communication between MDA-MB-231 VMO and VMT was compared. Results were filtered based on the probability of strong cell–cell communication, revealing that fibroblasts in the VMO communicate with EC through ANGPTL1–TEK (Tie2) signaling. Importantly, this signaling was significantly downregulated in the VMT (Additional file 1: Fig. A5C). Specifically, fibroblasts from the VMO were found to communicate with EC in the VMO through ANGPTL1–TEK signaling. To validate these interactions, we evaluated the expression of ANGPTL1 and TEK in the integrated dataset, both of which showed decreased expression in the VMT (Additional file 1: Fig. A5D). The potentially reduced TEK signaling observed in MDA-MB-231 VMT suggests an impairment in vascular maturation and stabilization, as TEK signaling is essential for these processes [33, 34]. And indeed, this is what we saw in the MDA-MB-231 VMTs (Fig. 1C).

A similar approach was undertaken for matched HCC1599 datasets, integrating the VMO and VMT datasets, which revealed four cell types: ECs, fibroblasts, pericytes, and tumor cells, as evidenced by the expression of cell type-specific marker genes (Additional file 1: Fig. A5E and F). The cell–cell communication between HCC1599 VMT and VMO was compared, with the filtered results including only interactions unique to the HCC1599 VMT dataset. Notably, one of the top pathways identified was ERBB3/HER3 signaling. To assess the strength of HER3/ERBB3 signaling in both VMO

and VMT HCC1599, clusterProfiler [35] was employed (Additional file 1: Fig. A5G). The analysis revealed that ERBB3 signaling was exclusively present in the VMT dataset, with fibroblasts and tumors acting as ligand sources for the receptor on the tumor population. To test the validity of these findings, we examined the expression of the ligand–receptor pair AREG-ERBB3 (Additional file 1: Fig. A5H). AREG expression was predominantly found in fibroblasts, with slightly higher expression from cells originating from the VMT. Conversely, ERBB3 expression was limited to cells derived from the VMT, primarily observed in the tumor population. Collectively, these findings support the hypothesis that AREG-ERBB3 signaling may contribute to tumor growth in HCC1599 VMT.

VMTs recapitulate the tumor microenvironment of clinical TNBC

To validate the clinical utility of the VMT as a tool for identifying therapeutically targetable pathways in TNBC, scRNA-seq datasets derived from primary TNBC samples were integrated with the VMT datasets. Single-cell transcriptomic comparison of VMTs with primary samples was conducted to verify whether the ANGPTL1–TEK and AREG-ERBB3 ligand–receptor pair correlations in MDA-MB-231 VMT and HCC1599 VMT and VMOs exhibited comparable patterns of decreased and increased expression, respectively, in clinical specimens. Patient samples from 3 publications [36–38] that included 17 TNBC patients were integrated with both the HCC1599 and MDA-MB-231 VMTs using scMerge [39] (Fig. 3). Integration of the datasets resulted in the identification of 12 distinct cell types (Fig. 3A), which were consistently observed across most samples (Fig. 3B, C). Cell type identities were assigned based on the expression patterns of established marker genes.

To conduct a focused comparison between the TNBC microenvironment of VMTs vs. clinical TNBC, we selectively extracted the fibroblasts, ECs, and epithelial cancer cells from each dataset (Fig. 3D). The subset data were then integrated to facilitate a direct comparison between the VMT and primary TNBC datasets. The cells predominantly formed clusters based on their cell type, and cells from each dataset seamlessly integrated with one another (Fig. 3D). Cell–cell communication was then performed using LIANA. When comparing the signaling between the clinical specimens and VMTs with the healthy control VMO (MDA-MB-231) dataset, it was observed that ANGPTL1–TEK signaling was more highly expressed in the VMO dataset (Fig. 3F), in comparison with either the VMT or the clinical samples, indicating that the expression patterns in the VMTs resembled those found in the clinical specimens. Similarly, when comparing the

signaling to the VMO (HCC1599) healthy control, we found that ERBB3 signaling was solely detected in the clinical and VMT integrated dataset (Fig. 3H), and not in the corresponding VMO control. The visualization of individual ligand–receptor pairs across datasets allowed us to assess the contribution of each dataset in terms of the cell types producing those transcripts (Fig. 3G–I). For ANGPTL1–TEK, there was a nominal expression of ANGPTL1 in the fibroblast populations that appeared slightly increased compared to the VMTs. For TEK, there seemed to be a somewhat increased expression in the Geldoff EC dataset; however, there was no significant interaction between angiopoietins and TEK. For the AREG and ERBB3 signaling pathway, there was expression of AREG across all the cell types and datasets, supporting its role in signaling to ERBB3, which is expressed exclusively in the tumor epithelial cells. Indeed, targeted HER3 therapeutic approaches may have potential in TNBC [40, 41]. The consistency observed between the VMT and clinical datasets indicates that these therapeutic options show promise for treating patients' disease.

Targeting dysregulated Angptl1/Tek tumor-EC signaling in MDA-MB-231 VMT normalizes vessels and improves perfusion

Previous studies have demonstrated the effectiveness of normalizing tumor vasculature in murine mammary carcinoma models using a vascular endothelial protein tyrosine phosphatase (VE-PTP) inhibitor, resulting in improved vessel perfusion and therapeutic delivery to tumors, thereby enhancing tumor killing. VE-PTP is a vascular endothelial cell-specific membrane phosphatase involved in dephosphorylation and consequent inactivation of the Tie2 receptor, leading to vessel destabilization [42]. Razuprotafib (AKB-9778) is a first-in-class VE-PTP inhibitor that induces Tie-2 activation in ECs to promote vascular maturation and enhance tumor perfusion [33]. Given the reduced ANGPTL1/TEK signaling in MDA-MB-231 VMT and clinical TNBC, which correlates with disrupted vasculature, our objective was to investigate the potential benefits of increasing TEK signaling in the tumor EC by blocking VE-PTP with razuprotafib. Thus,

we looked to integrate a vascular normalization strategy with conventional chemotherapy as a treatment approach for aggressive TNBC.

In order to establish the most effective concentration for treating MDA-MB-231 VMT with razuprotafib, a VE-PTP inhibitor known for its high potency in cell-free assay (IC50 = 17 pM [43]), we conducted a dose–response experiment. Two concentrations, 10 nM and 100 nM, were evaluated in MDA-MB-231 VMT over a 48-h period, and their vascular normalization capabilities were compared using vascular morphometry analysis, measuring average vessel length, lacunarity (the degree of empty space within the network area), and percent vessel area (Fig. 4A). Treatment with 10 nM razuprotafib resulted in a significant increase in average vessel length compared to the control group, along with a significant reduction in vascular lacunarity and a simultaneous increase in the percentage of vascular area within the treated VMTs, consistent with increased vessel density observed with razuprotafib-treated in vivo tumors [33]. These results highlight the inherent vascular disruption caused by MDA-MB-231 TNBC in the VMT and demonstrate the possibility of restoring intact vascular networks in the VMT by treatment with razuprotafib. Based on these data, we selected the lower concentration (10 nM) of razuprotafib for further experimentation.

We proceeded to conduct a time-course experiment in MDA-MB-231 VMT, where a 48-h treatment of 10 nM razuprotafib was added on day 5. Vascular morphometry analysis was performed every 48 h for 6 days following the treatment. At each time point examined, the administration of razuprotafib at 10 nM resulted in a significant improvement in average vessel length (Fig. 4B), mean vessel lacunarity (Fig. 4C), and vessel percent area compared to the control group that persisted for the duration of the experiment (Fig. 4D). Within just 24 h of treatment, there was a substantial ($\sim$ twofold) increase in vascular perfusion in MDA-MB-231 VMT compared to the untreated VMT (Fig. 4E). These findings are evident when examining fluorescent micrographs of MDA-MB-231 VMTs with and without razuprotafib treatment (Fig. 4F), where the pronounced improvement in perfusion of 70 kDa

(See figure on next page.)
Fig. 3 VMTs recapitulate the tumor microenvironment and tumor–stromal signaling pathways of clinical TNBC. **A** Integration of VMT HCC1599 and VMT MDA-MB-231 with clinical datasets from three different papers reveals numerous cell types found in patients, including immune cells. **B** Subset shows distribution of datasets in the integrated dimensional space. **C** Proportion of each cell type found in each dataset. **D** Integration of only the cell types found in the VMT **E** shows that the VMT maps well to patient data. **F** Angiopoietin-1 receptor (TEK/Tie2) cell–cell communication comparing the strength of the signaling between the VMO and VMT + clinical samples. Sender = cell type that produces the ligand, Receiver = cell type that produces the receptor. **G** Expression of TEK and TEK ligand angiopoietin like 1 (ANGPTL1) in the integrated dataset. Each bar refers to the expression in a single cell. **H** Erb-B2 Receptor Tyrosine Kinase 3 (ERBB3/HER3) cell–cell communication comparing the strength of the signaling between the VMO and VMT + clinical samples. **I** Expression of ERBB3 and ERBB3 ligand amphiregulin (AREG) in the integrated dataset
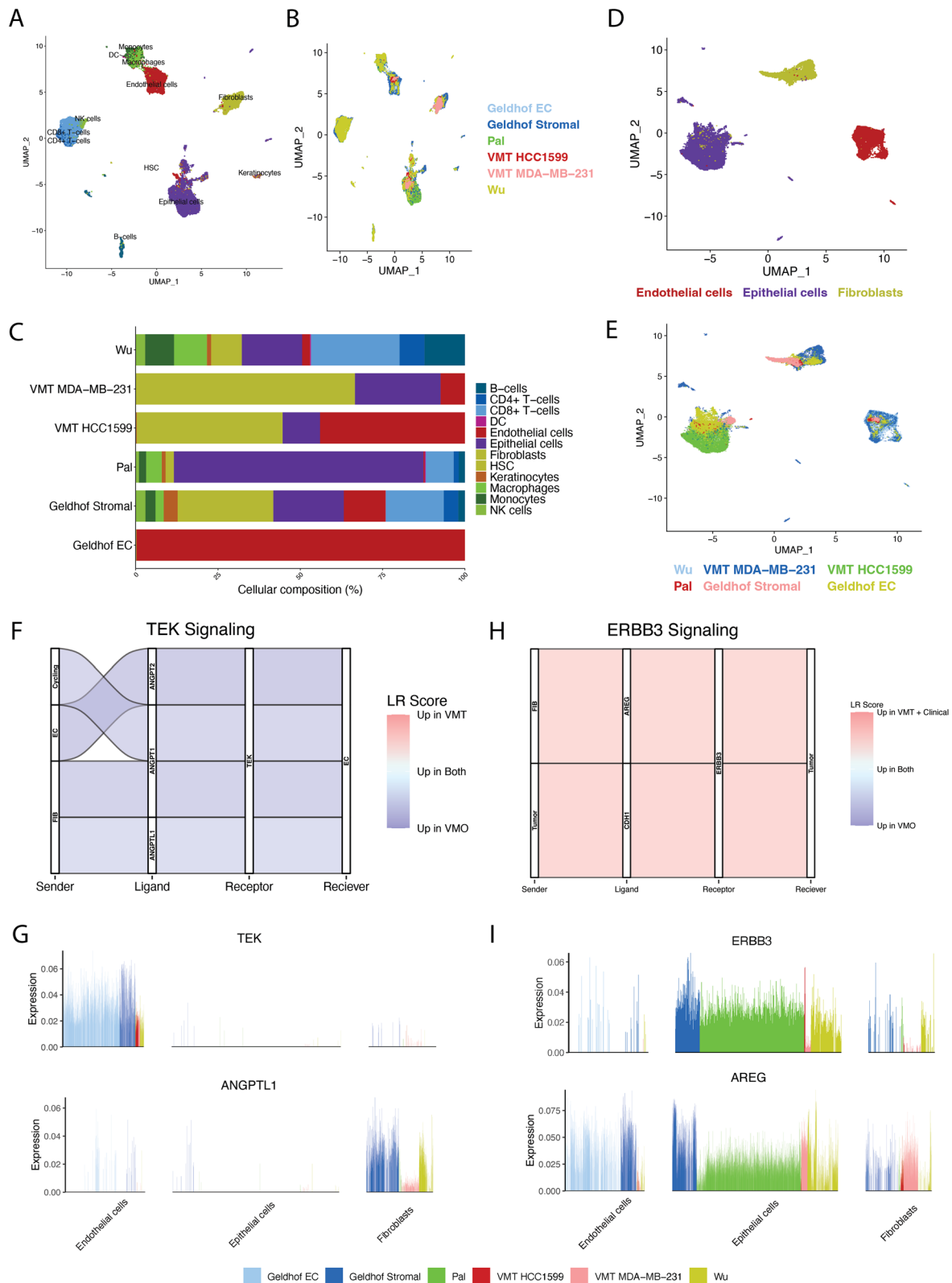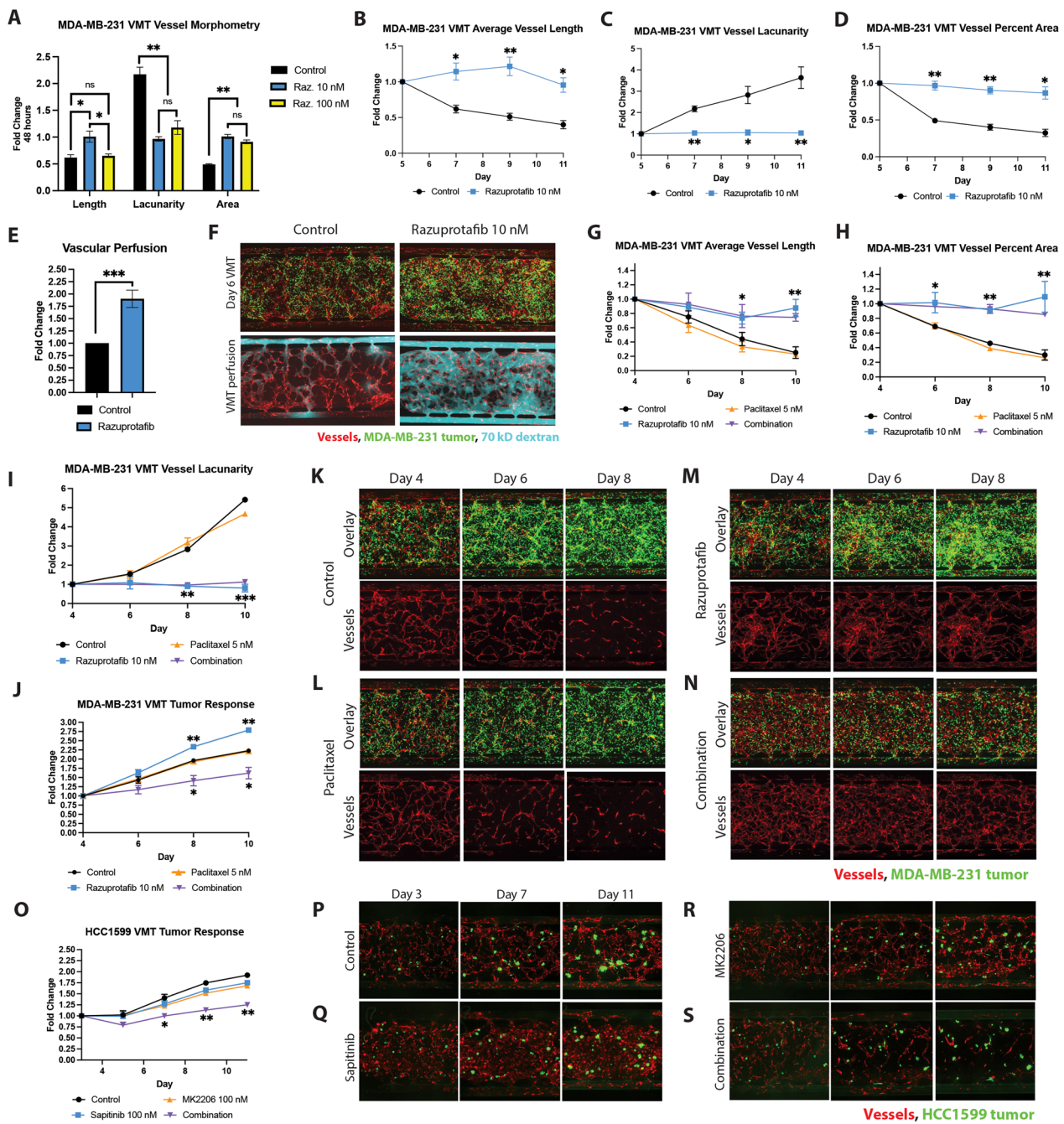
Fig. 3 (See legend on previous page.)

Fig. 4 Targeting dysregulated tumor–stromal signaling in MDA-MB-231 VMT and HCC1599 VMT improves therapeutic responses. **A** Bar plot showing relative fold change compared to control for different vascular morphometry measurements of MDA-MB-231 TNBC-associated vessel response to razuprotafib 10 nM and 100 nM dose administered in the VMT on day 5 of culture for 48 h. **B** Fold change in average vessel length in MDA-MB-231 VMT over the course of 6 days post-treatment with 10 nM razuprotafib. **C** Fold change in vessel lacunarity in MDA-MB-231 VMT over the course of 6 days post-treatment with 10 nM razuprotafib. **D** Fold change in vessel percent area in MDA-MB-231 VMT over the course of 6 days post-treatment with 10 nM razuprotafib. **E** Fold change in vascular perfusion with 70 kDa fluorescent dextran in MDA-MB-231 VMT 24 h post-treatment with 10 nM razuprotafib. **F** Fluorescent micrographs showing MDA-MB-231 VMT with and without razuprotafib 10 nM, with tumors in green and vessels in red. VMT are perfused on day 6 with 70 kDa fluorescent dextran (shown in cyan). **G** Fold change in average vessel length, **H** vessel percent area, **I** vessel lacunarity and (**J**) tumor growth in treated MDA-MB-231 VMT. **K** Fluorescent micrographs showing control, **L** paclitaxel-treated, **M** razuprotafib-treated, **N** and combination treated MDA-MB-231 VMT as overlay and vessel only images. **O** Fold change in tumor growth in treated HCC1599 VMT. **P** Fluorescent micrographs showing control, **Q** sapitinib-treated, **R** MK2206-treated, and **S** combination treated HCC1599 VMT. Note that stromal cells are present in the VMT but are not fluorescently labeled. *$p < 0.05$, **$p < 0.01$, ***$p < 0.001$

fluorescent dextran in the MDA-MB-231 VMT treated with razuprotafib can be clearly visualized.

Combining razuprotafib pretreatment with paclitaxel improves chemotherapeutic delivery and anti-cancer response in MDA-MB-231 VMT

In order to assess whether enhanced perfusion would translate into better delivery of therapeutics to the tumor, thereby increasing tumor cell death, pretreatment of MDA-MB-231 VMT with razuprotafib was performed prior to the administration of a dose of paclitaxel that was non-cytotoxic when used as a single-agent therapy in the VMT. Dosing was informed by 2D assay showing marginal effects on MDA-MB-231 tumor growth with 5 nM paclitaxel (Additional file 1: Fig. A6A). Notably, for each time point examined, there were no significant differences in average vessel length (Fig. 4G), vessel percent area (Fig. 4H), or vessel lacunarity (Fig. 4I) between MDA-MB-231 VMT treated with 5 nM paclitaxel and the control VMT. However, as both single-agent treatment and combination treatment with 5 nM paclitaxel, razuprotafib pretreatment exhibited a statistically significant improvement of the tumor-associated vasculature in all three metrics.

Tumor evaluation revealed that treatment with 5 nM paclitaxel alone did not result in a significant effect on tumor growth compared to the control group. However, when combined with razuprotafib pretreatment, there was a notable improvement in vessel perfusion, leading to enhanced drug delivery and a significant reduction in tumor growth by approximately 30% compared to the control (Fig. 4J). Interestingly, the single-agent treatment of razuprotafib resulted in a significant increase in MDA-MB-231 growth, likely due to improved nutrient supply to the tumor. These observations are consistent with the lack of significant effect of razuprotafib on MDA-MB-231 growth observed in 2D cytotoxicity assays either in the absence (Additional file 1: Fig. A6B) or presence of paclitaxel (Additional file 1: Fig. A6C).

Examination of the vascular networks in the control MDA-MB-231 VMT revealed progressive deterioration as the tumor grew and invaded the tumor microenvironment (Fig. 4K), and a similar disruption of vasculature was observed with paclitaxel treatment as the MDA-MB-231 tumor exhibited approximately a twofold increase in size throughout the duration of the experiment (Fig. 4L). In sharp contrast, the administration of razuprotafib resulted in tumor vessel normalization, demonstrated by the preservation of vascular network density despite a significant ~ 2.75-fold increase in tumor size (Fig. 4M). The combination treatment effectively prevented vascular lumen compression and pruning in the tumor microenvironment, facilitating improved drug

perfusion and heightened efficacy in tumor eradication (Fig. 4N).

HER3 inhibition synergizes with Akt1/2 inhibition in HCC1599 VMT

Recent clinical trials have highlighted the survival benefits of incorporating AKT inhibition in the treatment of TNBC [44, 45]. Furthermore, studies have shown that the combination of EGFR and HER3 antagonism with AKT inhibition enhances the anti-cancer effects [41, 46]. Considering the activated ERBB3 signaling pathway in HCC1599 VMT, characterized by elevated AREG expression in fibroblasts, and the absence of EGFR expression in HCC1599 [47], we conducted a treatment using sapitinib and MK-2206 to simultaneously inhibit HER3 and Akt1/2, respectively. Sapitinib is an ATP-competitive reversible inhibitor of EGFR/ErbB2/ErbB3, while MK-2206 is an allosteric inhibitor of Akt1/2.

As illustrated in Fig. 4O–S, when HCC1599 VMT was treated with 100 nM sapitinib and 100 nM MK-2206 individually, no significant cytotoxic activity against HCC1599 TNBC cells was observed. However, when combined, these treatments synergized to suppress tumor growth in the VMT, resulting in approximately 75% reduction in tumor burden compared to control and single-agent treatments. In contrast, HCC1599 exhibited no sensitivity to sapitinib, MK-2206, or the combination treatment in 2D culture (see Additional file 1: Fig. A6D–G) [48]. The insensitivity observed in 2D monocultures is likely attributable to the absence of paracrine signaling to ErbB3, which, in contrast, is captured within the VMT.

Differential protein expression between VMO and TNBC VMT substantiates the findings from scRNA-seq and treatment outcomes

Differential protein expression was verified between VMO and TNBC VMT, confirming downregulation in the Tie2 signaling axis for MDA-MB-231 and ErbB3 activation for HCC1599 that can be effectively overcome with targeted therapy (Fig. 5). Immunofluorescent (IF) staining of Tie2 reveals a downregulation of Tie2 in MDA-MB-231 VMT compared to the corresponding VMO, consistent with the single-cell RNA expression data (Fig. 5A, B). Upon closer examination of the VMO, a pronounced endothelial staining of Tie2 is evident when compared to untreated (control) MDA-MB-231 VMT (Fig. 5C, D). However, with 10 nM razuprotafib treatment, Tie2 levels in the MDA-MB-231 VMT show a significant $\sim$ twofold increase, restoring them to the levels observed in the VMO (Fig. 5E, F).

Similarly, IF staining for phosphorylated ErbB3/HER3 (pHER3) in HCC1599 VMT and the corresponding VMO illustrates heightened HER3 activation in HCC1599
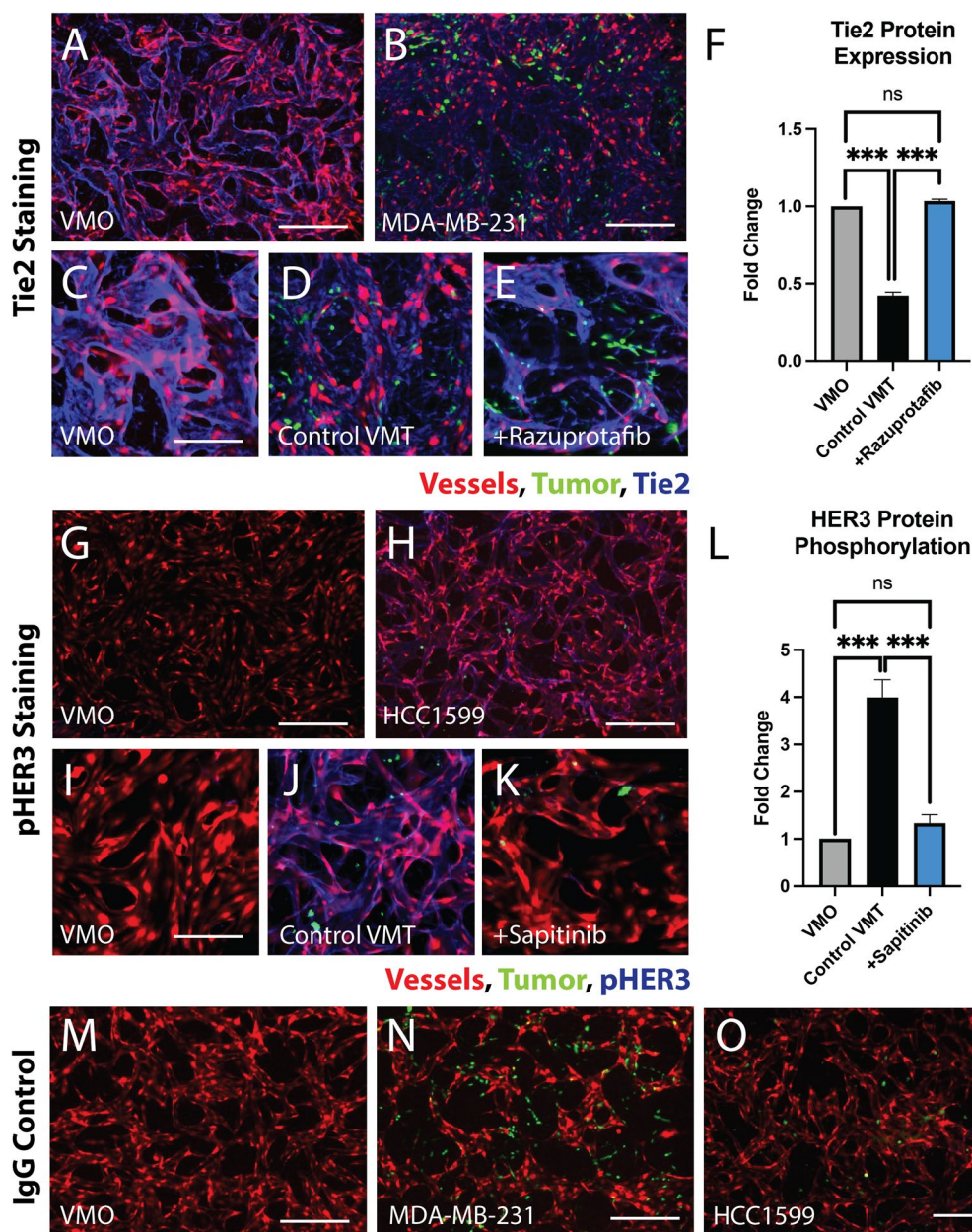
Fig. 5 Differential protein-level expression of drug targets is confirmed in VMOs and TNBC VMTs with and without treatment. **A** Tie2 staining of VMO and **B** MDA-MB-231 VMT shows differential expression. Vessels are red, tumor is green, and Tie2 protein is blue. Scale bars = 200 μm. **C** Zoom view of VMO stained with anti-Tie2 antibody. Scale bar = 100 μm **D** Zoom view of MDA-MB-231 VMT without treatment (control) stained with anti-Tie2 antibody. **E** Zoom view of MDA-MB-231 VMT treated with 10 nM razuprotafib and stained for Tie2. **F** Quantification of Tie2 protein expression in VMO, control MDA-MB-231 VMT, and razuprotafib-treated MDA-MB-231 VMT. **G** Phosphorylated ErbB3 (pHER3) staining of VMO and **H** HCC1599 VMT shows differential expression. Vessels are red, tumor is green, and pHER3 protein is blue. Scale bars = 200 μm. **I** Zoom view of VMO stained with anti-pHER3 antibody. Scale bar = 100 μm. **J** Zoom view of HCC1599 VMT without treatment (control) stained with anti-pHER3 antibody. **K** Zoom view of HCC1599 VMT treated with 100 nM sapitinib and stained for pHER3. **L** Quantification of HER3 protein phosphorylation in VMO, control HCC1599 VMT, and sapitinib-treated HCC1599 VMT. **M** Secondary-only IgG control VMO. Scale bar = 200 μm. **N** Secondary-only IgG control MDA-MB-231 VMT. Scale bar = 200 μm. **O** Secondary-only IgG control HCC1599 VMT. Scale bar = 200 μm. *ns* not significant, ***p < 0.0001

VMT, contrasting with minimal staining observed in the VMO (Fig. 5G–I). Intriguingly, a closer examination reveals that HER3 is activated not only in HCC1599 VMT tumors but also in associated vasculature (Fig. 5J). This increase in phosphorylated HER3 is nearly eradicated by treatment with 100 nM sapitinib, reverting

Hachey *et al. Breast Cancer Research*   (2024) 26:5

Page 13 of 20

to the baseline levels observed in the VMO (~ fourfold lower) (Fig. 5K–L). Control VMOs and TNBC VMTs with secondary-only IgG confirm the specificity of the antibodies for their targets, evident from the absence of background staining (Fig. 5M–O). These findings provide further mechanistic support to the scRNA-seq results and treatment outcomes.

Discussion

To study the TNBC TME, we established vascularized micro-tumors (VMTs) using two well-studied TNBC cell lines, MDA-MB-231 and HCC1599, along with ECs and primary stromal cells derived from histopathologically normal human breast tissue. Importantly, activated fibroblasts, despite their plasticity, demonstrate considerable heterogeneity in expression patterns, playing a role in cancer progression that varies depending on the tissue of origin [49]. Therefore, a notable strength of this study is the incorporation of primary stroma specific to breast tissue. MDA-MB-231 is an aggressive and poorly differentiated claudin-low molecular subtype TNBC cell line, known for its invasiveness and metastatic potential in various organs of mice [50]. Our findings demonstrate that the growth and migration of MDA-MB-231 cells in the VMT mirrors that seen in vivo (highly invasive) and leads to significant disruption of the vasculature, characterized by vessel regression, reduced vascular density, and impaired perfusion. These vascular changes observed in the VMT closely resemble the structural and functional vascular disruption seen in solid tumors, which often contributes to tumor progression by hindering effective delivery of anti-cancer therapies [8, 51, 52].

By analyzing the TNBC VMT compared to matched vascularized micro-organs (VMO), our aim was to uncover the molecular changes occurring in normal breast tissue-derived stromal cells when exposed to the TNBC microenvironment. Through single-cell transcriptomic analyses, we identified distinct cell–cell communication patterns and gene expression signatures within the tumor–stromal niche of MDA-MB-231. Notably, populations of fibroblasts exhibited gene signatures associated with cancer-associated fibroblasts (CAFs) as well as synthetic fibroblasts. The enriched fibroblast populations exhibited altered extracellular matrix organization processes that likely contributed to the destabilization of the tumor-associated vasculature. These characteristics observed within the tumor microenvironment have been previously associated with unfavorable outcomes in TNBC [11], underscoring the potential of utilizing the VMT to gain deeper insights into the intricate interplay within the TNBC TME.

Putative targets from cell–cell communication analyses were further validated for clinical relevance by comparing scRNA-seq data from VMTs/VMOs with publicly available scRNA-seq datasets derived from primary TNBC specimens. Significantly, the dysregulated ANGPTL1/TEK signaling pathway emerged as an intriguing therapeutic target with potential clinical significance since signaling through this ligand–receptor pair was found to be present in the VMO (MDA-MB-231) but reduced in the MDA-MB-231 VMT and TNBC clinical specimens. TEK, also known as Tie-2, is an endothelial tyrosine kinase receptor involved in vascular stabilization that is activated by angiopoietins, including Angiopoietin-related protein 1 (ANGPTL1) [42]. Its activity is regulated by VE-PTP, which dephosphorylates and inactivates it. Notably, in mouse models the VE-PTP inhibitor AKB-9778, or razuprotafib, has shown promise in stabilizing breast cancer vasculature and suppressing metastatic progression by sustaining Tie-2 activation [33]. Our findings using a human cell-based platform demonstrate that pharmacological inhibition of VE-PTP in the VMT can restore the structure and function of tumor vessels through upregulation of Tie2, leading to increased sensitivity of TNBC to low-dose chemotherapy with paclitaxel. However, it should be noted that as of the publication date, no clinical trials have been conducted to evaluate the effectiveness of razuprotafib in combination with anti-cancer agents, specifically in TNBC or any other cancer type [53]. This presents a promising opportunity for future clinical trials in TNBC, exploring the use of razuprotafib as a pretreatment strategy to enhance the delivery of cytotoxic drugs and immune cells to the tumor, ultimately leading to improved patient outcomes.

In our study, we observed that TNBC cells in both HCC1599 VMT and clinical specimens upregulate HER3 (ERBB3) in response to paracrine signaling from fibroblasts, mainly through increased expression of the ligand amphiregulin (AREG). HCC1599, a basal-like TNBC cell line, has been shown to better represent primary TNBC disease based on various '-omics' metrics compared to other cell lines [18, 19]. It also carries a BRCA2 gene mutation [47]. Interestingly, despite HER3 and Akt inhibitors showing little efficacy in HCC1599 monocultures as single agents or in combination, testing a low-dose combination of sapitinib and MK2206 in the HCC1599 VMT revealed synergistic anti-cancer effects. Sapitinib is a reversible ATP-competitive inhibitor of ErbB1/2/3 with an IC50 of 4 nM for ErbB3 in cell-free assays. Since HCC1599 lacks HER2 and EGFR expression [47], sapitinib presumably acts through ErbB3 inhibition in the VMT. We confirmed that administering sapitinib results in a significant decrease in phosphorylated HER3. Intriguingly, we detected activated HER3 in the endothelium of HCC1599 VMT, in addition to the tumor. Although this observation contrasts with our scRNA-seq

results, it is noteworthy that there is some expression of ERBB3 observed in endothelial cells derived from clinical datasets. The limitation in read depth could be a factor in detection, underscoring the need for further investigation.

Previous phase II trials of sapitinib in combination with paclitaxel for advanced breast cancer did not meet their primary endpoint of significantly increased duration of progression-free survival in the combination arm [54]. Similarly, a phase II trial evaluating MK2206-2HCl, a highly selective inhibitor of Akt1/2 [55], as a mono-therapy showed minimal therapeutic activity. However, a similar clinical trial assessing the combination of Akt inhibition as combination therapy with paclitaxel did show promising results with increased progression-free survival [45]. Notably, recent preclinical studies have highlighted the importance of targeting both HER3/EGFR and the downstream mediator Akt for optimal response in TNBC, particularly in TNBC cells with mutations in PIK3CA, AKT, or loss of PTEN [46, 56]. Although HCC1599 lacks these mutations, it does harbor mutations in PI3K/Akt pathway mediators, such as TNS1 and PIK3C2B [47], which may also play a role in predicting patient's response.

By faithfully reproducing essential elements of the tumor microenvironment, such as niche factors, dynamic cell–cell interactions, and the intricate tumor structure consisting of cancer cells, stromal cells, and vasculature, the VMT provides remarkable possibilities for modeling cancer within a physiologically relevant context. Recently, federal organizations, academic institutions, and industry experts have also recognized the value of tumor chips in expediting oncology drug discovery and streamlining preclinical development processes [57]. Our study further underscores the importance of faithfully reproducing the specific characteristics of the TNBC microenvironment to facilitate the discovery of innovative therapeutic strategies targeting reprogrammed stromal components. These efforts will be invaluable in accelerating the translation of findings from preclinical research into clinical trials, ultimately benefiting patients diagnosed with TNBC.

Conclusion

Through analysis of an advanced VMT model, clinically relevant drug targets associated with tumor-stromal interactions in TNBC were identified. The VMT faithfully reproduces critical components of the tumor microenvironment, encompassing tumor, stromal cells, and vasculature within a complex tissue structure. As such, the VMT can serve as a powerful tool for the research community and may also be useful for personalized medicine applications. In this study, effective reduction

of TNBC growth in the HCC1599 VMT model was achieved by targeting the activated AREG/ERBB3 signaling pathway, which is also activated in clinical TNBC. Similarly, in the MDA-MB-231 VMT model, targeting dysregulated ANGPTL1/TEK signaling, also observed in clinical TNBC, resulted in the normalization of dysfunctional vasculature and improved paclitaxel delivery, leading to reduced TNBC growth. These findings highlight the potential of modulating tumor–stromal crosstalk as a promising therapeutic strategy for TNBC. Finally, we note that the VMT platform is also ideally suited to studies of immune cell-based approaches to tumor management.

Methods
Microfluidic device fabrication

Device fabrication and loading has been described previously [13, 14, 16, 17, 58]. Briefly, a customized polyurethane master mold is fabricated using 2-part polyurethane liquid plastic (Smooth Cast 310, Smooth-On Inc.). A PDMS layer is then replicated from the master mold, holes are punched for inlets and outlets, and the platform is assembled in two steps. The PDMS layer is first attached to the bottom of a 96-well plate by chemical gluing and oxygen plasma treatment for 2 min. A 150-μm thin transparent membrane is then bonded to the bottom of the PDMS device layer by treating with oxygen plasma for an additional 2 min. The fully assembled platform is placed in a 60 °C oven overnight, covered with a standard 96-well plate polystyrene lid, and sterilized using UV light for 30 min prior to loading cells.

Collection and processing of primary human normal breast tissue

A breast tissue sample was acquired after ethical approval by the research center's Institutional Review Board (IRB) from the Cooperative Human Tissue Network (CHTN). The patient gave written, informed consent and shared the respective metadata. Inclusion criteria were that the sample was histopathologically normal. Tissue was processed as previously reported in [59]. The surgical specimen was washed in PBS, mechanically dissociated with scalpels, digested with 2 mg/mL collagenase I (Life Technologies, 17100-017) in DMEM (Corning, 10-013-CV) overnight, digested in 20 U/mL DNase I (Sigma-Aldrich, D4263-5VL) for 5 min, and centrifuged for 2 min at $150 \times g$. From the healthy patient specimen, supernatant was collected and centrifuged for 5 min at $500 \times g$ to isolate epithelial tissue chunks in the pellet. These were viably cryopreserved in DMEM with 50% FBS (Omega Scientific, FB-12) and 10% DMSO (vol/vol) before processing into single cells for flow cytometry. For flow cytometry, cells were stained using fluorescently

labeled antibodies for CD31 (eBiosciences, 48-0319-42), CD45 (eBiosciences, 48-9459-42), EpCAM (eBiosciences, 50-9326-42), CD49f (eBiosciences, 12-0495-82), Sytox-Blue (Life Technologies, S34857), PROCR (Biolegend, 351904), and PDPN (BioLegend, 337014).

Cell culture and microfluidic device loading
A published protocol was used to establish VMOs and VMTs [60]. To load cells, primary human normal breast stromal cells and ECFC-ECs were harvested and resuspended in fibrinogen solution at a concentration of 7×10^6 cells/mL and 3×10^6 cells/mL, respectively. MDA-MB-231 and HCC1599 TNBC cells were introduced at a concentration of 1×10^5 to 2×10^5 cells/mL to establish VMT. Fibrinogen solution was prepared by dissolving 70% clottable bovine fibrinogen (Sigma-Aldrich) in EBM2 basal media (Lonza) to a final concentration of 5 mg/mL. The cell–matrix suspension was mixed with thrombin (50 U/mL, Sigma-Aldrich) at a concentration of 3 U/mL, quickly seeded into the microtissue chambers, and allowed to polymerize in a 37 ℃ incubator for 15 min. Laminin (1 mg/mL, LifeTechnologies) was then introduced into the microfluidic channels through medium inlets and incubated at 37 ℃ for an additional 15 min. After incubation, culture medium (EGM-2, Lonza) was placed into the microfluidic channels and medium wells. Medium was changed every other day and hydrostatic pressure head re-established every day to maintain interstitial flow.

XTT assay for 2D cytotoxicity
Cell viability in 2D monolayer cultures ± treatment was quantified using an XTT assay according to the manufacturer's protocol (Sigma-Aldrich). Briefly, 5000 MDA-MB-231 or HCC1599 TNBC cells were seeded in triplicate in a 96-well plate and allowed to grow for 8 h prior to treatment with increasing doses of paclitaxel, razuprotafib, sapitinib, MK-2206 or combination treatments. XTT assays were performed after 48 h of drug exposure. A standard cell dilution was used to quantify total cell numbers. Cell viability was normalized to control wells without drug treatment.

Drug treatment in the VMT
Hydrostatic pressure was restored daily in the high-throughput platform, while medium was changed every 2 days. After culturing for 4–5 days to allow a perfused vasculature to form within each VMT, culture medium was replaced with medium containing the drugs at the desired concentration. Drugs were delivered to the tumor through the vascular bed via gravity-driven flow. Sapitinib (reversible, ATP-competitive inhibitor of EGFR, ErbB2 and ErbB3), MK-2206 2HCl (Akt 1/2/3 inhibitor),

and paclitaxel (microtubule stabilizer) were purchased from SelleckChem. Razuprotafib is a VE-PTP inhibitor that was purchased from MedChemExpress. MDA-MB-231 VMT were randomly assigned to one of four conditions: control (vehicle only), 5 nM paclitaxel, 10 nM razuprotafib, or combination 5 nM paclitaxel with 10 nM razuprotafib. VMT receiving razuprotafib were treated on day 4 for 24 h, followed by 48-h paclitaxel treatment for the combination condition or complete media for the single-agent condition. Single-agent paclitaxel was also treated for 48 h. HCC1599 VMT were treated on day 4–5 with one of the following: control (vehicle only), 100 nM sapitinib, 100 nM MK-2206 2HCl, or combination 100 nM sapitinib with 100 nM MK-2206 2HCl. Complete medium was replaced after 48 h. Fluorescent micrographs of VMT were taken every 48 h for 6 days post-treatment and growth of the tumor was quantified.

Fluorescence imaging and analyses
Fluorescence images were acquired with a Biotek Lionheart fluorescent inverted microscope using automated acquisition and standard 10× air objective. AngioTool software (National Cancer Institute) was used to quantify vessel area, vessel length, number of vascular junctions and endpoints in the VMT. ImageJ software (National Institutes of Health) was utilized to measure vessel diameter and measure the total fluorescence intensity (i.e., mean gray value) for each tumor image to quantify tumor growth. Each chamber was normalized to baseline. Vessels were perfused by adding 25 µg/mL FITC- or rhodamine-conjugated 70 kDa dextran to the medium inlet. Once the fluorescent dextran had reached the vascular network, time-lapse image sequences were acquired using a Nikon Ti-E Eclipse epifluorescence microscope with a 4× Plan Apochromat Lambda objective. Perfusion images were analyzed using ImageJ software by measuring change in fluorescence intensity within perfusable vessel regions and creating a composite score based on total perfusable vascular area. Tumor growth in the VMTs was quantified by measuring the total fluorescence intensity in the color channel representing the tumor cells. This takes into account both the area of the individual tumors and the depth, as thicker areas appear brighter. Any adjustments made to images are performed on the entire image, with all images in that experimental group adjusted to the same settings.

Immunofluorescent staining
VMOs and VMTs were fixed by flowing 4% paraformaldehyde into each device for 30 min at room temperature. After removing the membrane layer of each platform, chambers were then manually cut from the device layer and placed tissue-side down in a 24-well

tissue culture plate. Tissues were washed 3× 5 min with PBS on a rocker at 4 °C and permeabilized for 2× 10 min with 0.5% Triton-X in PBS. Blocking was performed for 1 h in 0.1% Triton-X in PBS with 10% goat serum. Antibody incubation was performed overnight at 4 °C. Tie2 was observed by staining with rabbit anti-human Tie2 polyclonal antibody (Abcam, EPR21915) at 1:100 followed by Alexa Fluor 488 goat anti-rabbit secondary antibody at 1:3000. Phosphorylated HER3/ErbB3 was observed by staining with rabbit anti-human ErbB3 antibody (phospho Y1289)(Abcam, EPR2325) at 1:100 followed by Alexa Fluor 568 goat anti-rabbit secondary antibody at 1:3000. Secondary-only IgG condition served as control.

Cell harvesting and single-cell sequencing

Media was aspirated from each well, and the high-throughput plates were inverted so that the device layer was facing up. The bottom membrane was gently peeled off the device to expose the tissue chambers. Devices were first washed with 500 μL of HBSS. To each device unit, 100 μL of TrypLE was added and allowed to sit as a bubble on top of the device while the plate was put back in the 37 °C incubator for 5 min. After digestion, tissue chambers were pipet into a 15-mL conical with EGM2 to neutralize the TrypLE. Digestion solution containing the dislodged tissues was centrifuged at 300 × g for 5 min at 4 °C to pellet single cells and whole tissues. Media was carefully aspirated, and a solution of 1 mg/mL (200 U/mL) collagenase III in HBSS was added to the undigested tissues. After gentle pipetting, the solution was allowed to sit for 2 min at room temperature before pipetting gently again to dissociate the gel. Digestion mix was washed with 10 mL of EGM2 and centrifuged at 300×*g* for 5 min at 4 °C. Cells were resuspended into 1X DPBS with 1% human serum albumin and passed through a pre-wetted 70-μm filter by spinning at 200×g for 1 min. Cells were counted and volume was adjusted so that total cells were at a concentration of 1000 cells/μL. Cellular suspensions were loaded onto a Chromium Single Cell Instrument (10× Genomics) to generate single-cell gel beads in emulsion (GEMs). GEMs were processed to generate cDNA libraries by using 10× Genomics v2 chemistry according to the Chromium Single Cell 3′ Reagents kits v2 user guide: CG00052 Rev B. Quantification of cDNA libraries was performed using Qubit dsDNA HS Assay kit (Life Technologies Q32851), high-sensitivity DNA chips (Agilent 5067-4626) and KAPA qPCR (Kapa Biosystems KK4824). Libraries were sequenced on an Illumina NovaSeq6000 to achieve an average of 50,000 reads per cell.

Transcriptome alignment and data processing of VMO and VMT libraries

FASTQ files for each library were aligned to an indexed GRCh38 reference genome using Cell Ranger (10× genomics) Count 3.1.0 to generate count matrices. Count matrices were loaded into RStudio (1.2.5042 version, R version 4.0.4 [61, 62]) and converted into a Seurat object using the Seurat R Package (version 4.0.0.9015) [63, 64]. Cells containing more than 15% mitochondrial RNA or with less than 200 features were removed. Additionally, genes not detected in at least 3 cells were trimmed. Data were normalized, the 2000 top variable features were found, and scaled using the NormalizeData, FindVariableFeatures, and ScaleData functions, respectively. Data were further normalized using the SCTransform function and the difference between cells in the S phase and G2M phase was regressed to help distinguish non-cycling from cycling cells. The 'SCT' assay slot was used for analyzing the individual datasets. Doublets were identified and removed using the DoubletFinder R package (version 2.0.3) [65]. A modified version of the chooseR R package [66] was used to generate silhouette scores for selecting the resolution. Clusters were labeled based on the expression of known markers (ECs: PECAM1, CDH5, VWF, KDR, CLDN5 [67], Fibroblasts: PDGFRA, PDG-FRB, COL1A1 [68], Stroma: PDGFRB, TPM1, ACTA2 [68], Cycling cells: MKI67 and TOP2A [69], and Tumor: KRT18 and EPCAM [70]), and cell types were later confirmed using the SingleR R package (version 1.4.1) [71]. Heatmaps were generated by filtering expression for each clustering by log2 fold change. Pathway analysis was performed using clusterProfiler [35] with the GO Biological Process 2021 database on the top 100 differentially expressed genes. The significance of key pathways was directly compared for each dataset.

Integration between VMO and VMT libraries

Individual libraries were integrated using the scMC Run-scMC R function and package (version 1.0.0) with default settings [21]. scMC removes the technical variation while preserving biological variation using variance analysis in an unsupervised manner. For integration, the 'RNA' slot was used for each library. After integration, cell types were assigned to individual cells based on the analysis of the individual libraries. UMAP for all of the datasets was generated with palette from the Polychrome R package (version 1.5.1) [72].

Processing publicly available patient libraries and integrating with VMT libraries

The Geldhof [38] libraries contain 8,433 ECs from 9 breast cancer patients and 26,515 total cells (GSE155109).

The EC enriched and stromal population count matrices were downloaded from the supplementary files. The Pal [37] libraries contain four libraries from triple-negative tumor with additional microenvironment cells (GSM4909284, GSM4909283, GSM4909282, and GSM4909281). The Wu [36] libraries contain 5 patient triple-negative breast cancer libraries that total 600 ECs (Broad SCP1106). The normalization and filtering of cells was performed as previously described. The clustree R package [73] was used to determine the optimal resolutions. The cells were assigned labels using the SingleR package, with the reference database limited to only include cell types that were mentioned in the original papers. The publicly available libraries and the VMT libraries were integrated with the scMerge (version 1.9.99) [39] R package using the scMerge::scMerge2 [74] with stably expressed genes calculated for the dataset to normalize the count matrices. Labels were assigned to each cell type using SingleR and 82 cells were removed due to not being assigned a label and not having a consensus cell type as its nearest neighbor. To integrate only the cell types present in the VMT libraries, the endothelial cells, epithelial cells, and fibroblasts as labeled by SingleR for each dataset were subset, and the subset libraries were integrated as described for the full libraries.

Cell–cell communication, visualization, and bar plot generation

The LIANA (version 0.0.1) [32] R package was used to compute the cell–cell communication between cell types. Possible interactions were pulled from the OmniPath database [75]. LIANA aggregates results from multiple cell–cell communication pipelines, and the results from the CellChat [76], Connectome [77], iTALK [78], NATMI [79], and SingleCellSignalR [80] pipelines were computed. Interactions that had a *p* value < 0.05 for CellChat were subset. Interactions were further filtered based on an aggregate rank < 0.05. Significant interactions were filtered based on expression in the VMO or VMT datasets. Individual receptor interactions were visualized using the CrossTalkeR R package (version 1.3.2) [81].

Pseudotime

Pseudotime was performed using Monocle v2 [31, 82]. Seurat data from the RNA slot was converted into a CellDataSet format following custom code provided by UC Irvine's Genomic High Throughput Facility. The expression for the data was modeled using a negative binomial distribution with the monocle::newCellDataSet function with the lower detection limit set to 0.5. The size factors and dispersion values that help with normalization and differential expression were computed, low-quality cells were filtered out, and cells were assigned to a pseudotime trajectory based on the total amount of transcriptional change. Branch expression analysis modeling (BEAM) was run to identify the branch-dependent genes. BEAM generates two negative binomial general linear models, one assuming the gene is branch independent and a second assuming the gene is branch dependent. The models are then fit to the pseudotime branch trajectories, and a likelihood ratio test determines if the genes are branch dependent or independent. Finally, a heatmap with the branch-dependent genes was generated using the monocle::plot_genes_branched _heatmap function. Genes with less than a 1e−45 *q* value (78 genes) were shown on the heatmap.

Statistical analyses

Data are represented as mean ± standard error of at least 9 replicates (at least 3 biological replicates with at least 3 technical replicates each). Comparison between experimental groups of equal variance was analyzed using an unpaired t-test and 95% confidence interval or one-way ANOVA followed by Dunnett's test for multiple comparisons. Statistical calculations were performed using GraphPad Prism 9.0 (GraphPad Software, San Diego, California USA, www.graphpad.com).

Abbreviations

CAF	Cancer-associated fibroblast
EC	Endothelial cell
ECM	Extracellular matrix
TME	Tumor microenvironment
TNBC	Triple-negative breast cancer
VMO	Vascularized micro-organ
VMT	Vascularized micro-tumor

Supplementary Information

The online version contains supplementary material available at https://doi.org/10.1186/s13058-023-01760-y.

Additional file 1. Supplemental figures.

Additional file 2: Table S1. Integrated dataset for VMOs and VMTs with all DEGs.

Additional file 3: Table S2. Pathway analysis for VMOs and VMTs (both MDA-MB-231 and HCC1599) by cell type.

Additional file 4: Table S3. Top 100 differentially expressed genes for fibroblast populations.

Hachey *et al. Breast Cancer Research*   (2024) 26:5

Page 18 of 20

Declarations

Ethics approval and consent to participate
A breast tissue sample was acquired after ethical approval by the research center's Institutional Review Board (IRB) from the Cooperative Human Tissue Network (CHTN). The patient gave written, informed consent and shared the respective metadata.

Consent for publication
All authors have reviewed and provided their consent for the publication of the content presented in this manuscript.

Competing interests
CCWH has an equity interest in Aracari Biosciences, Inc., which is commercializing some of the technology described in this paper. The terms of this arrangement have been reviewed and approved by the University of California, Irvine, in accordance with its competing interest policies.

References
1. Zagami P, Carey LA. Triple negative breast cancer: pitfalls and progress. NPJ Breast Cancer. 2022;8:95.
2. Siegel RL, Miller KD, Wagle NS, Jemal A. Cancer statistics, 2023. CA Cancer J Clin. 2023;73:17–48. https://doi.org/10.3322/caac.21763.
3. Yin L, Duan J-J, Bian X-W, Yu S-C. Triple-negative breast cancer molecular subtyping and treatment progress. Breast Cancer Res. 2020;22:61. https://doi.org/10.1186/s13058-020-01296-5.
4. Lin NU, et al. Clinicopathologic features, patterns of recurrence, and survival among women with triple-negative breast cancer in the national comprehensive cancer network. Cancer. 2012;118:5463–72.
5. Bianchini G, De Angelis C, Licata L, Gianni L. Treatment landscape of triple-negative breast cancer—expanded options, evolving needs. Nat Rev Clin Oncol. 2022;19:91–113. https://doi.org/10.1038/s41571-021-00565-2.
6. Zheng S, et al. Landscape of cancer-associated fibroblasts identifies the secreted biglycan as a protumor and immunosuppressive factor in triple-negative breast cancer. OncoImmunology. 2022;11:1–16. https://doi.org/10.1080/2162402X.2021.2020984.
7. Ding J-H, et al. Integrated analysis reveals the molecular features of fibrosis in triple-negative breast cancer. Mol Ther Oncol. 2022;24:624–35. https://doi.org/10.1016/j.omto.2022.02.003.
8. Mpekris F, et al. Combining microenvironment normalization strategies to improve cancer immunotherapy. Proc Natl Acad Sci. 2020;117:3728–37. https://doi.org/10.1073/pnas.1919764117.
9. Furukawa N, Stearns V, Santa-Maria CA, Popel AS. The tumor microenvironment and triple-negative breast cancer aggressiveness: shedding light on mechanisms and targeting. Expert Opin Ther Targets. 2022;26:1041–56. https://doi.org/10.1080/14728222.2022.2170779.
10. Hu D, et al. Cancer-associated fibroblasts in breast cancer: challenges and opportunities. Cancer Commun. 2022;42:401–34. https://doi.org/10.1002/cac2.12291.
11. Yu T, Di G. Role of tumor microenvironment in triple-negative breast cancer and its prognostic significance. Chin J Cancer Res. 2017;29:237–52.
12. Wang M, et al. Identification of cancer-associated fibroblast subtype of triple-negative breast cancer. J Oncol. 2022;2022:1–14.
13. Sobrino A, et al. 3D microtumors in vitro supported by perfused vascular networks. Sci Rep. 2016;6:31589. https://doi.org/10.1038/srep31589.
14. Phan DTT, et al. A vascularized and perfused organ-on-a-chip platform for large-scale drug screening applications. Lab Chip. 2017;17:511–20.
15. Hachey SJ, Hughes CCW. Applications of tumor chip technology. Lab Chip. 2018;18:2893–912. https://doi.org/10.1039/C8LC00330K.
16. Hachey SJ, et al. An in vitro vascularized micro-tumor model of human colorectal cancer recapitulates in vivo responses to standard-of-care therapy. Lab Chip. 2021;21:1333–51. https://doi.org/10.1039/D0LC01216E.
17. Hachey SJ, et al. A human vascularized microtumor model of patient-derived colorectal cancer recapitulates clinical disease. Transl Res. 2022;255:97–108.
18. Salvadores M, Fuster-Tormo F, Supek F. Matching cell lines with cancer type and subtype of origin via mutational, epigenomic, and transcriptomic patterns. Sci Adv. 2020;6:1–15. https://doi.org/10.1126/sciadv.aba1862.
19. Warren A, et al. Global computational alignment of tumor and cell line transcriptional profiles. Nat Commun. 2021;12:22. https://doi.org/10.1038/s41467-020-20294-x.
20. Stuart T, et al. Comprehensive integration of single-cell data. Cell. 2019;177:1888-1902.e21. https://doi.org/10.1016/j.cell.2019.05.031.
21. Zhang L, Nie Q. scMC learns biological variation through the alignment of multiple single-cell genomics datasets. Genome Biol. 2021;22:1–28.
22. Ziegler ME, Hatch MMS, Wu N, Muawad SA, Hughes CCW. mTORC2 mediates CXCL12-induced angiogenesis. Angiogenesis. 2016;19:359–71. https://doi.org/10.1007/s10456-016-9509-6.
23. Singer CF, et al. MMP-2 and MMP-9 expression in breast cancer-derived human fibroblasts is differentially regulated by stromal-epithelial interactions. Breast Cancer Res Treat. 2002;72:69–77. https://doi.org/10.1023/A:1014918512569.
24. Xiong S, Dong L, Cheng L. Neutrophils in cancer carcinogenesis and metastasis. J Hematol Oncol. 2021;14:173. https://doi.org/10.1186/s13045-021-01187-y.
25. Anelli V, Gault CR, Snider AJ, Obeid LM. Role of sphingosine kinase-1 in paracrine/transcellular angiogenesis and lymphangiogenesis in vitro. FASEB J. 2010;24:2727–38. https://doi.org/10.1096/fj.09-150540.
26. Yu Y, Wang W, Lu W, Chen W, Shang A. Inhibin *β*-A (INHBA) induces epithelial-mesenchymal transition and accelerates the motility of breast cancer cells by activating the TGF-*β* signaling pathway. Bioengineered. 2021;12:4681–96. https://doi.org/10.1080/21655979.2021.1957754.
27. Newman AC, Nakatsu MN, Chou W, Gershon PD, Hughes CCW. The requirement for fibroblasts in angiogenesis: fibroblast-derived matrix proteins are essential for endothelial cell lumen formation. Mol Biol Cell. 2011;22:3791–800. https://doi.org/10.1091/mbc.e11-05-0393.
28. Izutsu R, et al. AMIGO2 contained in cancer cell-derived extracellular vesicles enhances the adhesion of liver endothelial cells to cancer cells. Sci Rep. 2022;12:792. https://doi.org/10.1038/s41598-021-04662-1.
29. Osta WA, et al. EpCAM is overexpressed in breast cancer and is a potential target for breast cancer gene therapy. Cancer Res. 2004;64:5818–24.
30. Soysal SD, et al. EpCAM expression varies significantly and is differentially associated with prognosis in the luminal B HER2+, basal-like, and HER2 intrinsic subtypes of breast cancer. Br J Cancer. 2013;108:1480–7. https://doi.org/10.1038/bjc.2013.80.
31. Qiu X, et al. Reversed graph embedding resolves complex single-cell trajectories. Nat Methods. 2017;14:979–82. https://doi.org/10.1038/nmeth.4402.

32. Dimitrov D, et al. Comparison of methods and resources for cell–cell communication inference from single-cell RNA-Seq data. Nat Commun. 2022;13:3224. https://doi.org/10.1038/s41467-022-30755-0.

33. Goel S, et al. Effects of vascular-endothelial protein tyrosine phosphatase inhibition on breast cancer vasculature and metastatic progression. JNCI J Natl Cancer Inst. 2013;105:1188–201. https://doi.org/10.1093/jnci/djt164.

34. Braun LJ, et al. VE-PTP inhibition stabilizes endothelial junctions by activating FGD 5. EMBO Rep. 2019;20:1–18. https://doi.org/10.15252/embr.201847046.

35. Yu G, Wang LG, Han Y, He QY. ClusterProfiler: an R package for comparing biological themes among gene clusters. OMICS J Integr Biol. 2012;16:284–7.

36. Wu SZ, et al. Stromal cell diversity associated with immune evasion in human triple-negative breast cancer. EMBO J. 2020;39:1–20. https://doi.org/10.15252/embj.2019104063.

37. Pal B, et al. A single-cell RNA expression atlas of normal, preneoplastic and tumorigenic states in the human breast. EMBO J. 2021;40:1–23. https://doi.org/10.15252/embj.2020107333.

38. Geldhof V, et al. Single cell atlas identifies lipid-processing and immunomodulatory endothelial cells in healthy and malignant breast. Nat Commun. 2022;13:5511.

39. Lin Y, et al. ScMerge leverages factor analysis, stable expression, and pseudoreplication to merge multiple single-cell RNA-seq datasets. Proc Natl Acad Sci USA. 2019;116:9775–84.

40. Liu X, et al. Development of effective therapeutics targeting HER3 for cancer treatment. Biol Proced. 2019;21:5. https://doi.org/10.1186/s12575-019-0093-1.

41. Mishra R, Patel H, Alanazi S, Yuan L, Garrett JT. HER3 signaling and targeted therapy in cancer. Oncol Rev. 2018;12:45–62. https://doi.org/10.4081/oncol.2018.355.

42. Li G, Sachdev U, Peters K, Liang X, Lotze MT. The VE-PTP inhibitor AKB-9778 improves anti-tumor activity and diminishes the toxicity of interleukin 2 (IL-2) administration. J Immunother (Hagerstown, Md: 1997). 2019;42:237.

43. Shen J, et al. Targeting VE-PTP activates TIE2 and stabilizes the ocular vasculature. J Clin Investig. 2014;124:4564–76.

44. Xing Y, et al. Phase II trial of AKT inhibitor MK-2206 in patients with advanced breast cancer who have tumors with PIK3CA or AKT mutations, and/or PTEN loss/PTEN mutation. Breast Cancer Res. 2019;21:78. https://doi.org/10.1186/s13058-019-1154-8.

45. Schmid P, et al. Capivasertib plus paclitaxel versus placebo plus paclitaxel as first-line therapy for metastatic triple-negative breast cancer: the PAKT trial. J Clin Oncol. 2020;38:423–33. https://doi.org/10.1200/JCO.19.00368.

46. Ogden A, et al. Combined HER3-EGFR score in triple-negative breast cancer provides prognostic and predictive significance superior to individual biomarkers. Sci Rep. 2020;10:3009.

47. Broad Institute. Cancer dependency map. 2023. https://depmap.org/portal/. Accessed 02 July 2023.

48. Rees MG, et al. Correlating chemical sensitivity and basal gene expression reveals mechanism of action. Nat Chem Biol. 2016;12:109–16. https://doi.org/10.1038/nchembio.1986.

49. Kalluri R. The biology and function of fibroblasts in cancer. Nat Rev Cancer. 2016;16:582–98. https://doi.org/10.1038/nrc.2016.73.

50. Yoneda T, Williams PJ, Hiraga T, Niewolna M, Nishimura R. A bone-seeking clone exhibits different biological properties from the MDA-MB-231 parental human breast cancer cells and a brain-seeking clone in vivo and in vitro. J Bone Miner Res. 2001;16:1486–95. https://doi.org/10.1359/jbmr.2001.16.8.1486.

51. Sharma M, et al. Simultaneously targeting cancer-associated fibroblasts and angiogenic vessel as a treatment for TNBC. J Exp Med. 2021;218:e20200712.

52. Cazet AS, et al. Targeting stromal remodeling and cancer stem cell plasticity overcomes chemoresistance in triple negative breast cancer. Nat Commun. 2018;9:2897.

53. Information on clinical trials and human research studies. 2023. https://clinicaltrials.gov.

54. Johnston S, et al. Inhibition of EGFR, HER2, and HER3 signaling with AZD8931 in combination with anastrozole as an anticancer approach: phase II randomized study in women with endocrine-therapy-naïve advanced breast cancer. Breast Cancer Res Treat. 2016;160:91–9. https://doi.org/10.1007/s10549-016-3979-5.

55. Hirai H, et al. MK-2206, an allosteric Akt inhibitor, enhances antitumor efficacy by standard chemotherapeutic agents or molecular targeted drugs in vitro and in vivo. Mol Cancer Ther. 2010;9:1956–67.

56. Tao JJ, et al. Antagonism of EGFR and HER3 enhances the response to inhibitors of the PI3K-Akt pathway in triple-negative breast cancer. Sci Signal. 2014;7:1–10.

57. Low LA, Tagle DA. 'You-on-a-chip' for precision medicine. Expert Rev Precis Med Drug Dev. 2018;3:137–46. https://doi.org/10.1080/23808993.2018.1456333.

58. Moya ML, Hsu Y-H, Lee AP, Hughes CC, George SC. In vitro perfused human capillary networks. Tissue Eng Part C Methods. 2013;19:730–7. https://doi.org/10.1089/ten.tec.2012.0430.

59. Nee K, et al. Preneoplastic stromal cells promote BRCA1-mediated breast tumorigenesis. Nat Genet. 2023;55:595–606. https://doi.org/10.1038/s41588-023-01298-x.

60. Hachey SJ, Gaebler D, Hughes CCW. Establishing a physiologic human vascularized micro-tumor model for cancer research. J Vis Exp. 2023;199:e65865.

61. RStudio Team. RStudio: integrated development environment for R. Boston: RStudio, PBC; 2020. http://www.rstudio.com/.

62. R Core Team. R: a language and environment for statistical computing. Vienna: R Foundation for Statistical Computing; 2020. https://www.R-project.org/.

63. Butler A, Hoffman P, Smibert P, Papalexi E, Satija R. Integrating single-cell transcriptomic data across different conditions, technologies, and species. Nat Biotechnol. 2018;36:411–20. https://doi.org/10.1038/nbt.4096.

64. Satija R, Farrell JA, Gennert D, Schier AF, Regev A. Spatial reconstruction of single-cell gene expression data. Nat Biotechnol. 2015;33:495–502. https://doi.org/10.1038/nbt.3192.

65. McGinnis CS, Murrow LM, Gartner ZJ. DoubletFinder: Doublet detection in single-cell RNA sequencing data using artificial nearest neighbors. Cell Syst. 2019;8:329–37.

66. Patterson-Cross RB, Levine AJ, Menon V. Selecting single cell clustering parameter values using subsampling-based robustness metrics. BMC Bioinform. 2021;22:39. https://doi.org/10.1186/s12859-021-03957-4.

67. Ho M, et al. Identification of endothelial cell genes by combined database mining and microarray analysis. Physiol Genom. 2003;13:249–62. https://doi.org/10.1152/physiolgenomics.00186.2002.

68. Muhl L, et al. Single-cell analysis uncovers fibroblast heterogeneity and criteria for fibroblast and mural cell identification and discrimination. Nat Commun. 2020;11:3953. https://doi.org/10.1038/s41467-020-17740-1.

69. Gaudet P, et al. The gene ontology's reference genome project: a unified framework for functional annotation across species. PLoS Comput Biol. 2009;5:e1000431.

70. Kodack DP, et al. Primary patient-derived cancer cells and their potential for personalized cancer patient care. Cell Rep. 2017;21:3298–309.

71. Aran D, et al. Reference-based analysis of lung single-cell sequencing reveals a transitional profibrotic macrophage. Nat Immunol. 2019;20:163–72. https://doi.org/10.1038/s41590-018-0276-y.

72. Coombes KR, Brock G, Abrams ZB, Abruzzo LV. Polychrome: creating and assessing qualitative palettes with many colors. J Stat Softw Code Snippets. 2019;90:1–23.

73. Zappia L, Oshlack A. Clustering trees: a visualization for evaluating clusterings at multiple resolutions. GigaScience. 2018;7:giy083. https://doi.org/10.1093/gigascience/giy083.

74. Lin Y, Cao Y, Willie E, Patrick E, Yang J YH. Atlas-scale single-cell multi-sample multi-condition data integration using scMerge2. 2022. https://europepmc.org/article/PPR/PPR581962.

75. Türei D, et al. Integrated intra- and intercellular signaling knowledge for multicellular omics analysis. Mol Syst Biol. 2021;17:e9923. https://doi.org/10.15252/msb.20209923.

76. Jin S, et al. Inference and analysis of cell–cell communication using Cell Chat. Nat Commun. 2021;12:1088. https://doi.org/10.1038/s41467-021-21246-9.

77. Raredon MSB, et al. Computation and visualization of cell–cell signaling topologies in single-cell systems data using connectome. Sci Rep. 2022;12:4187. https://doi.org/10.1038/s41598-022-07959-x.

78. Wang Y, et al. iTALK: an R package to characterize and illustrate intercellular communication. 2019. https://doi.org/10.1101/507871.

79. Hou R, Denisenko E, Ong HT, Ramilowski JA, Forrest ARR. Predicting cell-to-cell communication networks using NATMI. Nat Commun. 2020;11:5011. https://doi.org/10.1038/s41467-020-18873-z.

80. Cabello-Aguilar S, et al. SingleCellSignalR: inference of intercellular networks from single-cell transcriptomics. Nucl Acids Res. 2020;48:e55–e55. https://doi.org/10.1093/nar/gkaa183.

81. Nagai JS, Leimkühler NB, Schaub MT, Schneider RK, Costa IG. CrossTalkeR: analysis and visualization of ligand–receptorne tworks. Bioinformatics. 2021;37:4263–5. https://doi.org/10.1093/bioinformatics/btab370.

82. Trapnell C, et al. The dynamics and regulators of cell fate decisions are revealed by pseudotemporal ordering of single cells. Nat Biotechnol. 2014;32:381–6. https://doi.org/10.1038/nbt.2859.

Publisher's Note